Article

Signatures of Vibrational and Electronic Quantum Beats in Femtosecond Coherence Spectra

Paul C. Arpin and Daniel B. Turner*

Cite This: *J. Phys. Chem. A* 2021, 125, 2425−2435

Read Online

ACCESS | 📊 Metrics & More | 📰 Article Recommendations

ABSTRACT: Femtosecond laser pulses can produce oscillatory signals in transient-absorption spectroscopy measurements. The quantum beats are often studied using femtosecond coherence spectra (FCS), the Fourier domain amplitude, and phase profiles at individual oscillation frequencies. In principle, one can identify the mechanism that gives rise to each quantum-beat signal by comparing its measured FCS to those arising from microscopic models. To date, however, most measured FCS deviate from the ubiquitous harmonic oscillator model. Here, we expand the inventory of models to which the measured spectra can be compared. We develop quantum-mechanical models of the fundamental, overtone, and combination-band FCS arising from harmonic potentials, the FCS of anharmonic potentials, and the FCS of a purely electronic dimer. This work solidifies the use of FCS for identifying electronic coherences that can arise in measurements of molecular aggregates including photosynthetic proteins. Furthermore, future studies can use the derived expressions to fit the measured FCS and thereby extract microscopic parameters of molecular potential-energy surfaces.
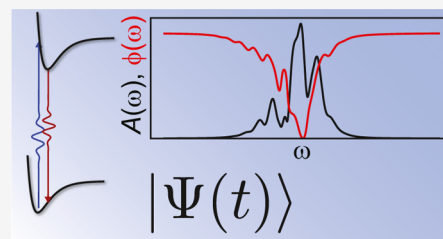
INTRODUCTION

The advent of broadband femtosecond laser pulses in the 1980s brought with it the observation of oscillatory signals arising from coherent quantum-beat signals in time-resolved spectroscopy measurements of atomic, semiconductor, and molecular samples.[1−6] Many research groups—especially those focused on molecules in the condensed phase—have observed and studied the intriguing amplitude and phase profiles of these oscillations found in transient-absorption spectra. Measurements and analyses of the quantum beats have been conducted on photosynthetic proteins,[7−10] heme proteins,[11] retinal-based complexes,[12−19] phytochrome pigment−protein samples,[20−23] conjugated polymers,[24,25] molecular aggregates,[26] and other molecular samples having intriguing photochemical or photophysical effects.[27−36] Additional studies have focused on solid-state samples including carbon nanotubes,[37] charge-transfer crystals,[38,39] and hybrid perovskites.[40] Other researchers have focused on developing theoretical models of the coherent oscillations, in particular the dynamics of a vibrational wavepacket on the excited electronic state. Researchers have used quantum-mechanical Gaussian wavepacket models,[41,42] an effective linear response approach,[43] a multimode phase-space analysis,[44] and a basis-truncation method.[45] The breadth of samples and phenomena studied using quantum-beat signals in femtosecond spectroscopy reflect the novel insights these methods yield into important physical phenomena including the mechanism of singlet exciton fission,[46,47] photoactivity mechanisms of signal-transduction proteins,[17] and the notion of nontrivial quantum effects in photosynthetic proteins.[48]

A common procedure for studying quantum beats is to conduct a conventional, spectrally resolved transient-absorption spectroscopy measurement using pulses that are impulsive, meaning having a duration shorter than the period of the quantum-beat frequency. The coherent oscillations of wavepackets—which arise physically through a difference-frequency mixing process between the various frequencies of the pump pulse—appear across a range of detection frequencies, and the oscillatory signals dephase typically on the order of 1 ps for molecular samples. After the measurement is performed, the quantum-beat signals are isolated and studied by a three-step procedure. First, one can fit and subtract population-decay signals. Second is Fourier transformation of the spectrally resolved signal over the pump−probe time interval. Third, one extracts the amplitude and phase profiles as a function of detection frequency for each oscillation frequency of interest. These profiles are known in the literature by several names, but here we refer to them as femtosecond coherence spectra (FCS). Even when a molecule has numerous normal vibrational modes, each typically has its own FCS, except in the case of accidental degeneracies. Figure 1 displays a simulated FCS for an excited-state vibrational wavepacket to illustrate the typical observations
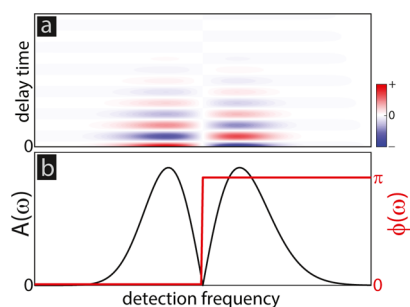
Figure 1. (a) Oscillatory quantum-beat signals often arise in femtosecond, spectrally resolved transient-absorption spectroscopy through a difference-frequency mixing process. (b) The amplitude and phase profiles, $A(\omega)$ and $\phi(\omega)$, respectively, at a selected oscillation frequency are known as an FCS. Previous studies explored the sharp amplitude node and abrupt π phase shift that are diagnostic for the fundamental oscillations of a vibrational wavepacket in a harmonic potential. In this work, we significantly expand on the spectral signatures of vibrational and electronic coherences.

of a sharp amplitude node and a discrete π phase shift, both occurring at the emission wavelength that corresponds to the peak of the fluorescence spectrum.

Despite these efforts, the measured FCS often do not match the predictions arising from theoretical models. In many measurements, extra nodes and phase shifts are present. In other cases, the phase shift is highly structured or less than π. Some of these differences likely arise from experimental imperfections such as pump scatter, pulse chirp,[4,30] or contamination from ground-state wavepackets.[49] Other differences likely arise from photoactivity or nontrivial excited-state topography.

One plausible explanation for the mismatch between the theoretical predictions and the measured spectra is that studies thus far have almost exclusively focused on fundamental vibrational oscillations arising from harmonic potentials, yet potentials can be anharmonic. In addition, TA measurements can contain quantum beats arising from overtones and combination bands. Therefore, in this contribution, we derive analytic FCS expressions for these models. To add breadth, we also derive the FCS of a purely electronic dimer.

Femtosecond transient-absorption spectroscopy and the FCS analysis method have been used to study a wide variety of photochemical and photophysical phenomena. More recently, a related four-wave mixing method known as two-dimensional electronic spectroscopy (2D ES) has become more widely adopted for studying quantum-beat signals.[50,51] 2D ES provides resolution along the excitation and emission frequency dimensions,[52] in contrast to TA spectroscopy, which provides resolution along the emission dimension. Both methods have a variable pump–probe time delay interval, and consequently the analogue of an FCS in 2D ES is known as a "beating map". 2D ES offers enhanced resolution or separation of signals in comparison to TA but at a considerable cost of complexity: 2D ES measurements are significantly more challenging to perform in the laboratory and more difficult to analyze and interpret than TA spectra. A second difference is that pump pulses that span the absorption spectrum will typically suppress the confounding and less-informative ground-state wavepacket signals in TA spectroscopy.[27,29,53] In contrast, signals from both ground-state and excited-state wavepackets appear in 2D ES. Therefore, FCS remains an important spectroscopic method for studying the mechanisms that give rise to quantum-beat signals.

The outline of the paper is as follows. In the Theoretical section we present the general expression for an excited-state vibrational wavepacket using the doorway-window method. In the Results and Discussion, we present the key contributions, which are analytic expressions for the FCS for five models of quantum-beat signals, and we use simulations to identify diagnostic features for each mechanism. We conclude by listing some future mechanisms that remain to be explored.

■ THEORETICAL

Vibrational Wavepacket Dynamics. Our previous work used a doorway-window method that was based on a classical window function.[45] That work encountered challenges for anharmonic potentials. Therefore, here we use a window function based on energies of the transitions between the vibrational sublevels in each electronic potential and analytic expressions for the Franck–Condon factors to produce fully quantum-mechanical expressions for the FCS of the vibrational models.[53] Specifically, we use a window function (W) for the excited state $|e\rangle$, which is the stimulated-emission term in this doorway-window picture because in the impulsive, resonant excitation condition relevant to modern measurements using ultrabroadband pump pulses, ground-state wavepacket oscillations are suppressed.[27,29,53]

The expression for the density matrix of a time-dependent wavepacket in an excited state is given by

$$\rho(\tau) = \sum_{n,n'}^{N,N} c_{n,0} c_{n',0}^* e^{-i(E_{n'}-E_n)\tau/\hbar} |e, n\rangle\langle e, n'| \tag{1}$$

where n and n' are both vibrational eigenstates of the excited electronic state and where the coefficients $c_{i,j}$ are Franck–Condon factors, values that indicate the degree of overlap between two vibrational eigenstates from distinct electronic states displaced along the internuclear separation variable, q, by an amount Δ. They can be written as

$$c_{n,m} \equiv FC_{n,m} = \int dq \psi_{e,n}(q - \Delta)\psi_{g,m}(q) \tag{2}$$

Equation 1 allows for an arbitrary set of energy levels. To compute the signal that arises in transient absorption spectroscopy, we will also need the window operator

$$W(\omega) = \sum_{n,n'}^{N,N} |e, n\rangle\langle e, n'| \sum_m^N c_{n,m} c_{n',m}^* \left[\frac{1}{\omega - \omega_{n',m} + i\gamma/2} - \frac{1}{\omega - \omega_{n,m} - i\gamma/2} \right] \tag{3}$$

where m indexes the vibrational eigenstate of the ground electronic state, $\omega_{a,b} = (E_a - E_b)/\hbar$, and γ is the dephasing of the emitted optical coherence signal. The transient-absorption signal as a function of detection frequency variable, ω, and time delay variable, τ, is given by

$$S(\omega, \tau) \propto Tr[W(\omega)\rho(\tau)] \tag{4}$$

where the trace is evaluated on the basis of the vibrational eigenstates on the excited electronic state, $Tr[\hat{O}] = \sum_n \langle e,n|\hat{O}|e,n\rangle$. Inserting the expressions—using distinct indices for the sums in ρ and W—and further simplification yields

$$S(\omega, \tau) \propto \sum_{n,n',m}^{N} c_{n,m}^{*} c_{n',m} c_{n,0} c_{n',0}^{*} \left[\frac{1}{\omega - \omega_{n',m} + i\gamma/2} \right.$$

$$\left. - \frac{1}{\omega - \omega_{n,m} - i\gamma/2} \right] e^{-i(E_{n'} - E_n)\tau/\hbar} \tag{5}$$

where N represent the upper limit of all summation variables. Finally, we must calculate the FCS. The first step is Fourier transformation of the signal function over the time-delay variable τ to yield an oscillation-frequency variable that we denote by ω_2

$$M(\omega; \omega_2) = \mathscr{F}_\tau [S(\omega, \tau)]$$

$$= \sum_{n,n',m}^{N} c_{n,m}^{*} c_{n',m} c_{n,0} c_{n',0}^{*} \left[\frac{1}{\omega - \omega_{n',m} + i\gamma/2} - \frac{1}{\omega - \omega_{n,m} - i\gamma/2} \right]$$

$$\times 2\pi \delta(\omega_2 - (E_{n'} - E_n)/\hbar). \tag{6}$$

where ω is the detection frequency variable and ω_2 is the oscillation frequency variable. This expression provides an analytic route to the FCS without numeric computation of the quantum-beat signals followed by Fourier transformation. Further progress can be made only after choosing a model for the potential-energy surfaces and selecting a particular oscillation frequency, ω_2, of interest.

The approximations made to derive the doorway-window expressions are appropriate for many transient-absorption measurements on condensed phase samples but do limit the range of validity of the results herein. In particular, the doorway-window approach is valid for well-separated pump and probe pulses[53] and will not characterize dynamics occurring during pulse overlap. In addition, the specific form of the density matrix and window function chosen give the "bare spectrum", which is the signal due to the response of the molecule independent of the details of the laser pulse. This is valid in the limit that the laser pulse is short compared to the nuclear dynamics of the sample but long compared to the dephasing of the electronic transition.[53] The FCS can be calculated for laser pulses that deviate from these approximations by performing a convolution between the laser pulse and the bare spectrum as a temporal convolution along the delay time axis for a long pulse or as a spectral convolution along the probe frequency axis for a short pulse.[53,54] A long pulse would uniformly suppress the amplitude of high-frequency oscillations. A short pulse would broaden the lines of the individual transitions in the probe frequency resolved spectrum.

Harmonic Potential. We first choose to use the harmonic oscillator, whose potential-energy function is written as $\hat{V}(q) = 1/2 m\omega_0^2 \hat{q}^2$, where $\omega_0 = \sqrt{k/m}$ is the angular frequency for a mass m and force constant k. This expression assumes that the equilibrium position of the oscillator is $q_0 = 0$. A parameter used below is the curvature, α, given by $\alpha = \sqrt{m\omega_0/\hbar}$, which has units of inverse length. In fact, $\alpha = 1/x_0$, where x_0 is the classical turning point for the $n = 0$ eigenfunction. The well-known energy levels are $E_n = (n + 1/2)\hbar\omega_0$. To make the notation explicit, we state the eigenfunctions, $\psi_n(q) = N_n \exp(-\alpha^2 q^2/2) H_n(\alpha q)$, where the normalization constant is given by $N_n = \sqrt{\frac{\alpha}{2^n n!}} \pi^{-1/4}$ and the $H_n(\alpha q)$ is a Hermite polynomial of order n.

Morse Potential. The potential-energy function for the Morse oscillator[55,56] is given by $\hat{V}(x) = D_e (1 - e^{-a(x-x_e)})^2$, where x_e is the equilibrium bond distance, D_e is the well depth (the

dissociation energy plus the zero-point energy), and a is inversely related to the width of the potential well. We define a key unitless parameter, λ, as $\lambda = \sqrt{2mD_e}/(a\hbar)$, and an effective frequency of the oscillator at the equilibrium position, $\omega_0^{\text{eff}} = \sqrt{\frac{2D_e a^2}{m}}$. The finite number of bound eigenstates of the Morse oscillator is $n \in \{0, 1, 2, ..., [\lambda + 1/2]\}$, where the square braces, $[\kappa]$, indicate a floor function such that this value is the largest integer smaller than κ. The energy levels of the Morse oscillator are

$$E_n = \left(n + \frac{1}{2} \right) \hbar \omega_0^{\text{eff}} - \frac{\left[\left(n + \frac{1}{2} \right) \hbar \omega_0^{\text{eff}} \right]^2}{4D_e} \tag{7}$$

The classical turning points of the $n = 0$ eigenfunction for the Morse oscillator are given by $x_0 = x_e - \frac{1}{a}\ln(1 \pm \sqrt{E_0/D_e})$, where E_0 is the energy of the $n = 0$ eigenfunction given by eq 7 and where we will use $x_e = 0$. Due to the asymmetry of the Morse potential, there will be two distinct solutions, in contrast to the harmonic oscillator potential wherein the turning points were simply $\pm x_0$. Therefore, when normalizing the displacement, we will use $\overline{x_0}$, which represents the mean of the two x_0 values for the Morse oscillator.

The eigenfunctions of the Morse oscillator can be written as

$$\psi_{n,\lambda}(x) = \sqrt{a} M_{n,\lambda} (2\lambda w)^{\lambda - n - 1/2} e^{-\lambda w} L_n^{(2\lambda - 2n - 1)}(2\lambda w) \tag{8}$$

where $w = e^{-a(x-x_e)}$, $L_n^{(\kappa)}(z)$ is a generalized Laguerre polynomial, and the normalization constant is given by

$$M_{n,\lambda} = \left(\sum_{j=0}^{n} \frac{\Gamma(2\lambda - 2n - 1 + j)}{j!} \right)^{-1/2} \tag{9}$$

■ RESULTS AND DISCUSSION

Fundamental Oscillations of a Harmonic Oscillator. Numerous authors have provided analytic solutions for Franck–Condon factors for a pair of harmonic oscillators. We choose to use the result from Iachello and Ibrahim.[56] The full expression for the Franck–Condon factors—their eq 2.9—is not reproduced here. We adjusted their notation such that m and n indicate vibrational sublevels of the ground and excited electronic states, respectively, and then we simplified for the case of identical curvatures, $\alpha = \alpha'$. The expression for each Franck–Condon factor simplifies tremendously to

$$\text{FC}_{n,m}^{\text{HO}} = (-1)^m e^{-\tilde{\Delta}^2/4} \sqrt{\frac{n!m!}{2^{n+m}}} \tilde{\Delta}^{n+m}$$

$$\sum_{l=0}^{\min[n,m]} \left(-\frac{2}{\tilde{\Delta}^2} \right)^l \frac{1}{l!(n-l)!(m-l)!} \tag{10}$$

where $\tilde{\Delta} \equiv \Delta/x_0$ is a normalized displacement parameter.

This expression allowed us to derive the complete expression for the FCS for the fundamental oscillations. Because $\hbar\omega_0 = E_{n+1} - E_n$, we choose $n' = n + 1$ and $\omega_2 = \omega_0$ and find that

$$M(\omega; \omega_0) = e^{-\tilde{\Delta}^2} \sum_{n,m}^{N} m! \left(\frac{\tilde{\Delta}^2}{2}\right)^{2n+m+1} A_{n,m}(\tilde{\Delta}) A_{n+1,m}(\tilde{\Delta})$$

$$\left[\frac{1}{\omega - \omega_{n+1,m} + i\gamma/2} - \frac{1}{\omega - \omega_{n,m} - i\gamma/2}\right] \tag{11}$$

where the auxiliary functions are given by

$$A_{n,m}(\tilde{\Delta}) = \sum_{l=0}^{\min[n,m]} \left(-\frac{2}{\tilde{\Delta}^2}\right)^l \frac{1}{l!(n-l)!(m-l)!} \tag{12}$$

The expression yields several physical insights. First, the factor of $m!$ indicates that there will be more nonzero coefficients in m than n for a set value of $\tilde{\Delta}$. Second, higher values of n and m become non-negligible as $\tilde{\Delta}$ increases, which matches the intuition that as the displacement is increased, higher-lying vibrational states should have non-negligible coefficients. Third, negative-valued Franck–Condon factors must arise from the $(-1)^l$ component in the auxiliary functions. Fourth, the two Lorentzian terms produce sequences of peaks that will overlap and interfere when the summations over m and n are performed. Fifth, the displacement enters this expression everywhere as $\tilde{\Delta}^2$; thus negative and positive displacement values will produce identical FCS.

Our simulations begin with an analysis of how the coefficients and frequencies vary as $\tilde{\Delta}$ changes for the FCS at the fundamental vibrational frequency for the harmonic oscillator model. Each peak in an FCS is created by a sum of, potentially, many terms arising from both Lorentzian functions that have distinct frequencies for a given (n, m) combination. For our chosen set of simulation parameters, $m = 0.5$, $\hbar = 1$, $\omega_{eg} = 400$, and $\omega_0 = 9$, we show the frequency matrices as well as the matrix representing the product of Franck–Condon factors for two values of $\tilde{\Delta}$, in Figure 2. The matrices representing different cases of the product of Franck–Condon factors indeed confirm that the values are non-negligible for more values of m than n.

We analyze the case of $\tilde{\Delta} = 0.1$ in more detail. The matrices reveal that there will be four non-negligible terms. The first term contributes a positive-amplitude coefficient applied to the Lorentzian at $\omega_{n=0,m=0} = \omega_{eg} = 400$, and the second is a negative-
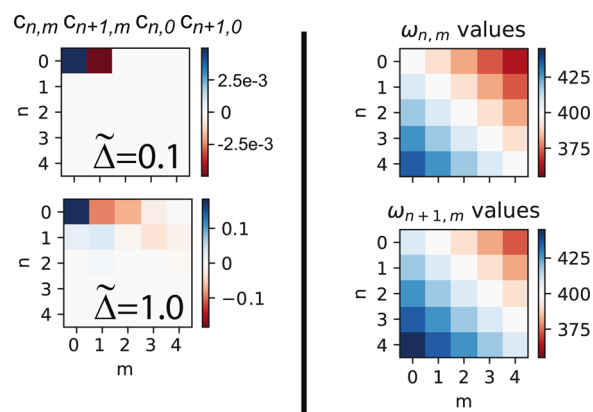
amplitude coefficient applied to the Lorentzian at $\omega_{n=0,m=1} = \omega_{eg} - \omega_0 = 391$. The third and fourth are, respectively, positive-amplitude and negative-amplitude coefficients applied to the Lorentzian at $\omega_{n+1=1,m=0} = \omega_{eg} + \omega_0 = 409$ and $\omega_{n+1=1,m=1} = \omega_{eg} = 400$.

These matrices reveal the number, location, and amplitude of each Lorentzian peak that will compose a full FCS for the fundamental oscillations of the harmonic oscillator. The peaks in the FCS are distinct when $\gamma \ll \omega_0$, see top panels of Figure 3. The vertical axes are normalized in all instances except for the phase, which is in radians. The Lorentzian terms each produce two non-negligible peaks for $\tilde{\Delta} = 0.1$. The total spectrum is the sum, and because two of the four peaks overlap, there are three distinct peaks in the total spectrum. At larger displacements, more peaks appear. For example, we plot the FCS in the upper right panel of Figure 3 for $\tilde{\Delta} = 1.0$, where now six distinct peaks are visible. The fundamental transition at ω_{eg} is not the strongest peak due to destructive interference among the contributing terms. These data reveal that as the displacement increases, more vibronic transitions become non-negligible, an explanation familiar from steady-state spectroscopy methods.

The small dephasing values are related to gas-phase spectroscopy measurements. However, FCS are generally used to study condensed-phase systems. Therefore, we evaluate larger dephasing values where the distinct peaks can overlap and further interfere. The bottom two panels in Figure 3 reveal that the overlap among the peaks leads to FCS that nearly reproduce the classical-window spectra[45] in which the amplitude node is sharp, the peaks on either side of the node are exactly equal in amplitude, and the abrupt π phase shift occurs for all values of $\tilde{\Delta}$. These features are reproduced in the $\tilde{\Delta} = 0.1$ case in Figure 3, but the $\tilde{\Delta} = 1.0$ spectrum has an unanticipated asymmetry between the two peak amplitudes as well as smoother variation in the phase profile.

We studied this asymmetry further by evaluating the relative peak heights across a range of displacements, $0.05 \leq \tilde{\Delta} \leq 2.5$ for $\gamma = 2\omega_0$ and $\gamma = 10\omega_0$. Smaller dephasing values led to spectra that contained multiple distinct peaks, complicating this analysis. The data presented in Figure 4 reveal that the relative peak heights vary at most by about 20%, which occurs at $\tilde{\Delta} = 1.0$.

We attempted to derive an analytic expression for the relative peak heights as a function of $\tilde{\Delta}$, γ, and ω_0. However, due to the complications arising from the multiple summations in eq 11, we were unable to find a general solution. We anticipate that under certain approximations, an analytic expression might be achieved; however, we did not pursue the analytic solution further and proceeded to a numeric evaluation of limiting cases. We found that the FCS converge to the classical result when $\gamma/\omega_0 \approx 10\tilde{\Delta}$. The explanation is that the dephasing sets the range of possible emission energies between each vibrational level of the excited and ground electronic states. When $\gamma < \omega_0$, the transitions are discrete and therefore the quantum-window approach applies. When γ is large, all transition frequencies are allowed, which is the classical interpretation. To support that assessment, Figure 5 displays the vibrational FCS for $\tilde{\Delta} = 1.0$ when $\gamma = 10\omega_0$. The interference among essentially all of the contributing terms makes the abrupt phase shift return and produces peaks that now have symmetric heights.

Overtone Oscillations of a Harmonic Oscillator. Sensitive TA measurements can reveal signals arising from overtones,[35,57] and therefore we derive the FCS for the first overtone of the harmonic oscillator by choosing $n' = n + 2$ and selecting $\omega_2 = 2\omega_0$. The result is
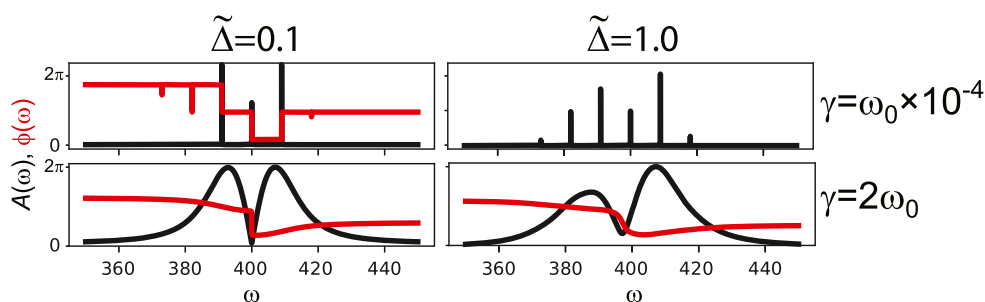

Figure 2. Components for FCS expression for the fundamental frequency of a harmonic oscillator, for each (n, m) combination. (left) Variation in the product of Franck–Condon factors, $c_{n,m}c_{n+1,m}c_{n,0}c_{n+1,0}$, for two selected values of $\tilde{\Delta}$ and (right) emission frequency of each term arising from the Lorentzian functions.

Figure 3. FCS for fundamental oscillations of the harmonic oscillator model for $\tilde{\Delta} \in \{0.1, 1.0\}$ when $\gamma \in \{\omega_0 \times 10^{-4}, 2\omega_0\}$. The number of terms increases with increasing displacement, and the larger dephasing values can converge to the classical-window result.
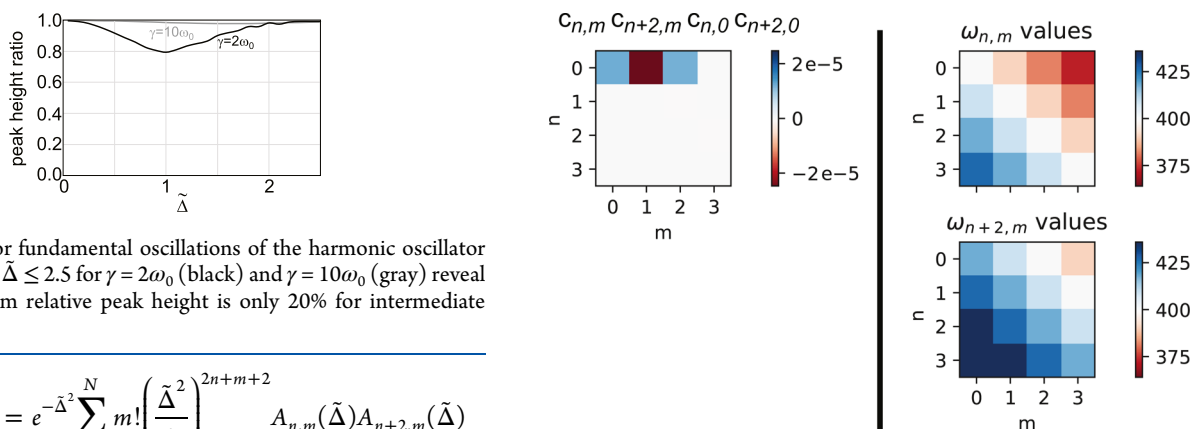

Figure 4. FCS for fundamental oscillations of the harmonic oscillator model for $0.05 \leq \tilde{\Delta} \leq 2.5$ for $\gamma = 2\omega_0$ (black) and $\gamma = 10\omega_0$ (gray) reveal that the maximum relative peak height is only 20% for intermediate dephasing.

$$M(\omega; 2\omega_0) = e^{-\tilde{\Delta}^2} \sum_{n,m}^{N} m! \left(\frac{\tilde{\Delta}^2}{2}\right)^{2n+m+2} A_{n,m}(\tilde{\Delta}) A_{n+2,m}(\tilde{\Delta})$$

$$\left[\frac{1}{\omega - \omega_{n+2,m} + i\gamma/2} - \frac{1}{\omega - \omega_{n,m} - i\gamma/2}\right] \quad (13)$$

There are three differences between the FCS expressions of the harmonic oscillator fundamental and its first overtone: the exponent on the $(\tilde{\Delta}^2/2)$ term is slightly different, the auxiliary function involves $n + 2$ rather than $n + 1$, and the one Lorentzian term will shift all the peaks by an extra factor of ω_0. The final aspect significantly affects the interference among peaks.

Figure 6 contains the Franck−Condon coefficient product matrix for $\tilde{\Delta} = 0.1$ and the frequency matrices for the first overtone of the harmonic oscillator model. For this displacement, three (n, m) combinations make non-negligible contributions to the VCS, and the $\omega_{n+2,m}$ Lorentzian shifts the frequencies one additional unit of ω_0 compared to the $\omega_{n+1,m}$ Lorentzian of the fundamental harmonic oscillator FCS.

Based on the Franck−Condon and frequency matrices for $\tilde{\Delta} = 0.1$ presented in Figure 6, we anticipate that the $\omega_{n,m}$ and $\omega_{n+2,m}$ terms will each produce three peaks and overlap at only one emission frequency. Therefore, we anticipate that the FCS for this displacement value will have a pattern of five distinct peaks centered at ω_{eg}. In contrast, the fundamental frequency FCS at

Figure 6. Product of Franck−Condon factors for $\tilde{\Delta} = 0.1$ and emission frequency of each term arising from the Lorentzian functions, for each (n, m) combination of the $2\omega_0$ overtone.

the same displacement value had a total of four non-negligible terms producing a total of three peaks centered at ω_{eg}.

We display example FCS for the overtone in Figure 7 for both narrow and wide peaks widths at $\tilde{\Delta} = 0.1$ and 1.0 as representative examples. The narrow peak spectrum for $\tilde{\Delta} = 0.1$ shows that indeed the Lorentzian with $\omega_{n+2,m}$ shifts to higher frequencies relative to that of $\omega_{n+1,m}$ for the fundamental frequency case. This shift causes interference effects that are distinct from those of the fundamental frequency. The $\gamma = 2\omega_0$ FCS show that some peak structure and phase dependence develop.

These simulations demonstrate that overtones can be distinguished from fundamental frequencies by the distinctive pattern of dual nodes and phase shifts and, furthermore, the presence of an overtone can be confirmed by the presence of the fundamental peak having the correct phase and amplitude profiles at half the frequency of the overtone. This analysis is straightforward to extend to higher overtones.

Combination Band Oscillations of a Harmonic Oscillator. Like overtones, some TA measurements can reveal peaks
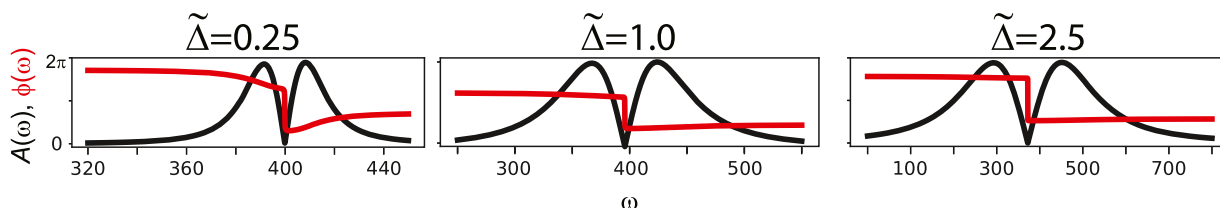

Figure 5. Overlap and interference of peaks when $\gamma/\omega_0 = 10\tilde{\Delta}$ converges to the corresponding classical-window FCS.
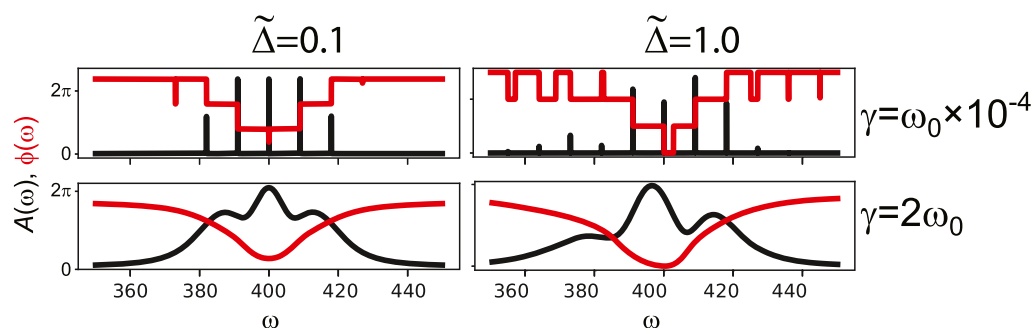
Figure 7. FCS of the first overtone, $\omega_2 = 2\omega_0$, for $\tilde{\Delta} = 0.1$ and 1.0 for narrow (top) and wide (bottom) peak widths. The three-peak pattern and the phase symmetry appear to be diagnostics of an overtone FCS.
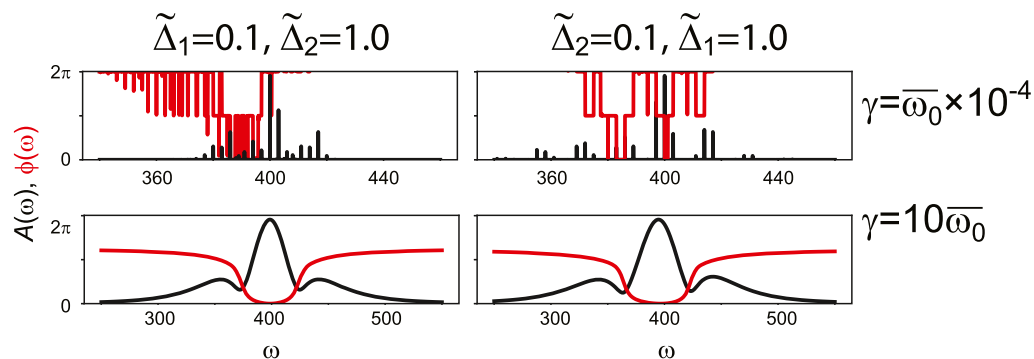

Figure 8. FCS of a combination band for $\omega_{0_1} = 3$, $\omega_{0_2} = 14$. Displacements and dephasings are as indicated. The symmetry of the combination-band FCS resembles the symmetry of the overtone FCS for these parameters.

arising from combination bands.[35,57] These oscillations require a potentially complicated two-dimensional simulation. We made three simplifications. The first is that the ground and excited states will have the same pair of distinct curvatures: α_1 and α_2. The second is that there is no Duschinsky rotation so that the full Franck–Condon factor can be written as the product of the two 1D Franck–Condon factors. Third, we ignore "accidental" degeneracies that are possible but unlikely. The primary combination band of interest is the sum of the two fundamental oscillation frequencies and therefore we select $\omega_2 = \omega_{0_1} + \omega_{0_2}$.

Extrapolating from the analysis above, we can write the general expression for the 2D FCS as

$$M(\omega; \omega_2) = \sum_{\substack{n_1,n_2,m_1 \\ n_1',n_2',m_2}}^{N} c_{n_1,n_2;m_1,m_2} c_{n_1',n_2';m_1,m_2}^* c_{n_1,n_2;0,0} c_{n_1',n_2';0,0}^*$$

$$\times \left[\frac{1}{\omega - \omega_{n_1',n_2';m_1,m_2} + i\gamma/2} \right.$$

$$\left. - \frac{1}{\omega - \omega_{n_1,n_2;m_1,m_2} - i\gamma/2} \right]$$

$$\times 2\pi\delta(\omega_2 - (E_{n_1',n_2'} - E_{n_1,n_2})/\hbar)$$

(14)

where m_1 and m_2 index the ground-state vibrational levels along internuclear displacement directions 1 and 2, and where n_1, n_2, n_1', and n_2' index the excited-state vibrational levels along the 1 and 2 directions. Due to our interest in $\omega_2 = \omega_{0_1} + \omega_{0_2}$, we set $n_2' = n_2 + 1$ and $n_1' = n_1 + 1$. The FCS expression becomes

$$M(\omega; \omega_{0_1} + \omega_{0_2}) = e^{-\tilde{\Delta}_1^2 - \tilde{\Delta}_2^2} \sum_{n_1,n_2,m_1,m_2}^{N} m_1! m_2!$$

$$\left(\frac{\tilde{\Delta}_1^2}{2} \right)^{2n_1+m_1+1} \left(\frac{\tilde{\Delta}_2^2}{2} \right)^{2n_2+m_2+1}$$

$$\times A_{n_1,m_1}(\tilde{\Delta}_1) A_{n_1+1,m_1}(\tilde{\Delta}_1) A_{n_2,m_2}(\tilde{\Delta}_2)$$
$$A_{n_2+1,m_2}(\tilde{\Delta}_2)$$

$$\times \left[\frac{1}{\omega - \omega_{n_1+1,n_2+1;m_1,m_2} + i\gamma/2} \right.$$

$$\left. - \frac{1}{\omega - \omega_{n_1,n_2;m_1,m_2} - i\gamma/2} \right]$$

(15)

where $\tilde{\Delta}_1$ and $\tilde{\Delta}_2$ are the normalized displacements along the 1 and 2 dimensions, respectively.

We then performed simulations under distinct sets of displacements and dephasing parameters. Figure 8 presents some results. The peak patterns of the combination-band FCS somewhat resemble those of the overtone FCS. The similarity arises most clearly when the dephasing approaches that of the classical window function, here $\gamma = 10\overline{\omega_0}$, where $\overline{\omega_0} = (\omega_{0_1} + \omega_{0_2})/2$, which have the dual node and phase shift structure similar to the overtone FCS.

This set of simulations seems to indicate that the combination-band FCS are always fairly symmetric. However, intermediate dephasing produced FCS having extremely asymmetric and disordered profiles. We present in Figure 9 a simulated harmonic oscillator combination-band FCS with
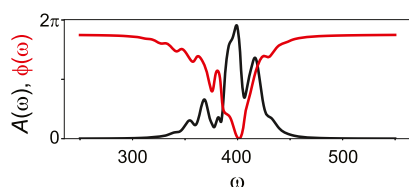
Figure 9. FCS of a combination band for $\omega_{0_1} = 3$, $\omega_{0_2} = 14$, $\gamma = 2\overline{\omega_0}$ and $\Delta_1 = 0.1$, and $\Delta_2 = 1.0$. The intermediate level of dephasing produces complicated phase and amplitude profiles.

$\gamma = 2\overline{\omega_0}$. The structure of the amplitude profile has one primary node and numerous other minima. The phase profile is extremely structured, and we do not attempt to interpret all of the features. Despite the potentially very complicated FCS that can arise for combination bands, they are likely to be distinguished because a combination band will appear at an oscillation frequency that is the sum of two fundamental oscillations.

Morse Oscillator. In previous work, we found that the Morse potential could provide insights into the effects of anharmonicity on the FCS.[45] That analysis, however, required great care and careful selection of parameters because the difference between Morse potentials is a double-valued function. Therefore, we pursue its use with the quantum-mechanical window function.

For the Franck–Condon factors, we again modify an expression presented by Iachello and Ibrahim.[56] Specifically, their eq 4.5 is a form for the case of identical but displaced potentials that can be expressed in a consistent notation here as

$$
FC_{n,m}^{MO} = M_{m,\lambda} M_{n,\lambda} \zeta^{\lambda-n-1/2} \left(\frac{2}{1+\zeta}\right)^{\xi}
$$
$$
\sum_{k,k'=0}^{n,m} \left[\frac{(-1)^{k+k'}}{k!k'!} \binom{\xi+n}{m-k'}\binom{\xi+m}{n-k} \xi^k \left(\frac{2}{1+\xi}\right)^{k+k'} \right.
$$
$$
\left. \Gamma(\eta) \right]
\tag{16}
$$

where we have assumed that $\lambda = \lambda'$, where we have defined variables

$$
\tilde{\Delta} = (x_e' - x_e)/\overline{x_0}
\tag{17a}
$$

$$
\zeta = e^{-a\overline{x_0}\tilde{\Delta}}
\tag{17b}
$$

$$
\eta = 2\lambda - n - m + k + k' - 1
\tag{17c}
$$

$$
\xi = 2\lambda - m - n - 1
\tag{17d}
$$

for succinctness, where we use binomial coefficients given by

$$
\binom{a}{b} = \frac{\Gamma(a+1)}{\Gamma(b+1)\Gamma(a-b+1)}
\tag{18}
$$

and where the auxiliary function is given by

$$
M_{n,\lambda} = \left(\sum_{j=0}^{n} \frac{\Gamma(2\lambda - 2n - 1 + j)}{j!} \right)^{-1/2}.
\tag{19}
$$

Developing the full analytic expression for the FCS expression for the Morse oscillator poses new complications. The energy-level spacing is not a constant like it was for the case of the

harmonic oscillator, and therefore many peaks will appear as a function of ω_2 and potentially multiple combinations of n' and n will contribute for a selected ω_2 value. Therefore, we calculate the wavepacket oscillations at every ω_2 value by performing the additional sum over n' rather than setting n' to a specific value like we did for the harmonic oscillator cases

$$
M^*(\omega; \omega_2) = \sum_{n',n,m}^{n,\lambda,\lambda} c_{n,m} c_{n',m}^* c_{n,0} c_{n',0}^* \left[\frac{1}{\omega - \omega_{n',m} + i\gamma/2} \right.
$$
$$
\left. - \frac{1}{\omega - \omega_{n,m} - i\gamma/2} \right] \left(\frac{1}{(\omega_2 - \omega_{n',n})^2 - \gamma_2} \right)
\tag{20}
$$

where γ_2 sets the width of each peak as a function of ω_2 and each $c_{i,j}$ is given by eq 16. We select only $n' > n$ because we are not interested in negative-frequency or zero-frequency oscillations. Then, we select the ω_2 value that corresponds to the most intense oscillations. For small values of $\tilde{\Delta}$, this frequency arises from the two lowest energy eigenstates, $\omega_{0,1} = (E_1 - E_0)/\hbar$ and therefore, $M(\omega, \omega_{0,1}) = M^*(\omega; \omega_2)|_{\omega_{0,1}}$.

Performing the FCS simulations for the Morse oscillator requires a bit of care because the $\Gamma(\eta)$ term in eq 16 becomes numerically unstable at high values of λ. Recall that λ is effectively the number of bound eigenfunctions in each potential. This tends to make the initial values of the $\{n', n, m\}$ indices reliable, which produces reasonable spectra when $\tilde{\Delta}$ is small enough such that the higher-lying eigenfunctions have negligible Franck–Condon factors. Larger values can also produce reliable spectra after examination and selection of each term.

We present the full FCS as a function of ω_2 and ω when $\tilde{\Delta} = 0.1$ and $\tilde{\Delta} = 0.4$ in Figure 10. The main oscillations occur at $\omega_2 = \omega_{0,1}$, which is the frequency that corresponds to a wavepacket composed of the $n = 0$ and $n = 1$ eigenstates on the excited electronic potential. For the $\tilde{\Delta} = 0.4$ case, a minor oscillation occurs at $\omega_2 \approx \omega_{0,1}/0.6$, which corresponds under these parameters to a wavepacket composed of the $n = 1$ and $n = 2$ eigenstates. At larger displacements, oscillations occur at other frequencies lower than $\omega_{0,1}$ that correspond to wavepackets of other eigenstate combinations. For example, there are oscillations at $\omega_2 \approx 0.6\omega_{0,1}$ in the case of $\tilde{\Delta} = 0.4$. These peaks are not the main focus of this work but could be of interest in future studies.

In principle, we could compute each (n', n) combination that will lead to oscillations at a selected ω_2 frequency. In practice, however, some distinct peaks could appear near the selected ω_2 frequency and, due to nonzero peak widths, affect its FCS. Therefore, we perform the full calculation and then select the primary oscillation frequency, $\omega_2 = \omega_{0,1}$, and display the conventional FCS in Figure 11 for $\gamma = 2\omega_0^{\text{eff}}$. The amplitude and phase profiles are essentially vertical lineouts from Figure 10, and they resemble those of the harmonic oscillator simulations, with the key distinction that the asymmetry between peak heights become dramatic for what seem to be modest values of $\tilde{\Delta}$. Simulations with the dephasing increased to $\gamma = 10\omega_0^{\text{eff}}$, Figure 12, recovered the sharp amplitude node and abrupt π phase shift for $\tilde{\Delta} = 0.1$; in fact the spectrum is indistinguishable from that of the harmonic oscillator. This fits the intuition that at small displacements, the wavepacket is composed of only the two lowest energy eigenstates in both models.[45] In all cases, however, even modest displacements reveal sharply asymmetric peak heights and complicated phase profiles. These results show that
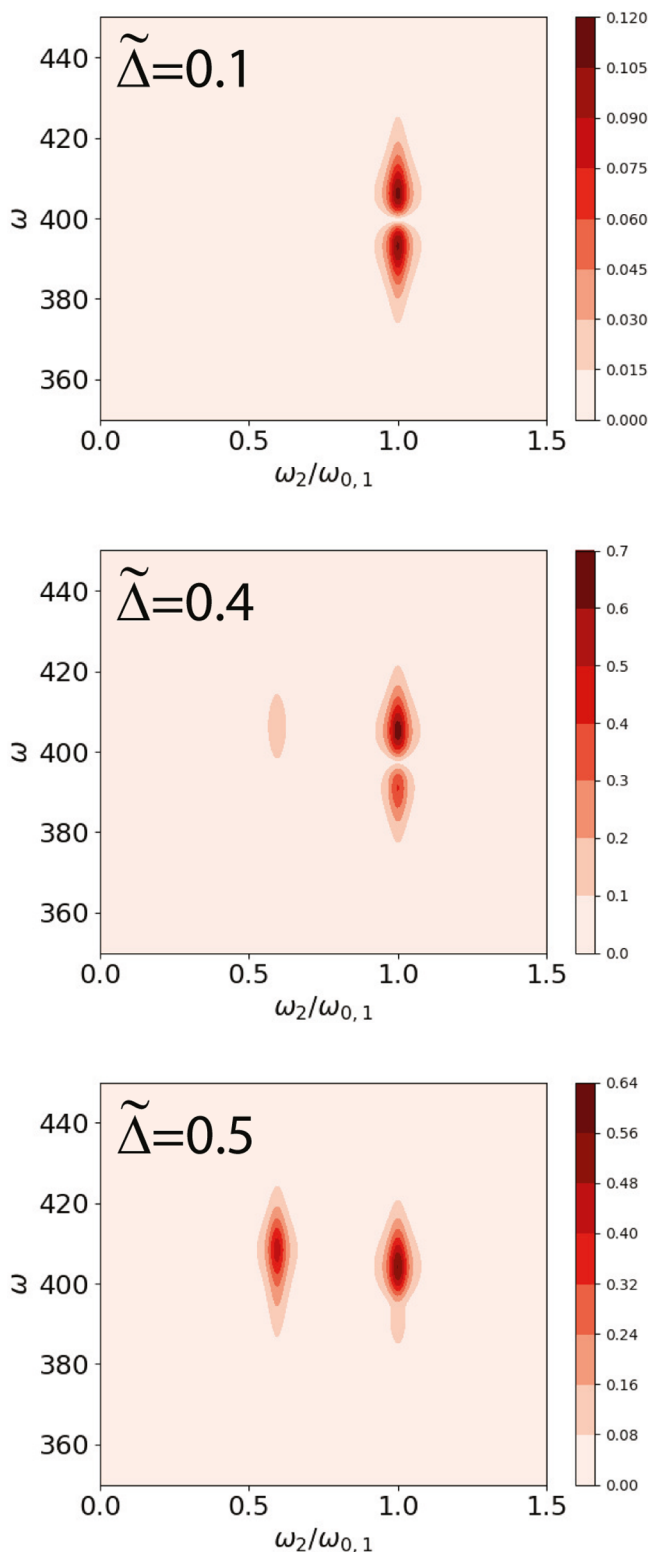
Figure 10. Morse oscillator FCS for indicated $\tilde{\Delta}$ values for $\omega_0^{eff} = 9$ and in which the n and m sums used all 12 bound states. The horizontal axis is normalized to the $\omega_{0,1}$ frequency. The vertical axis is the emission frequency, ω.
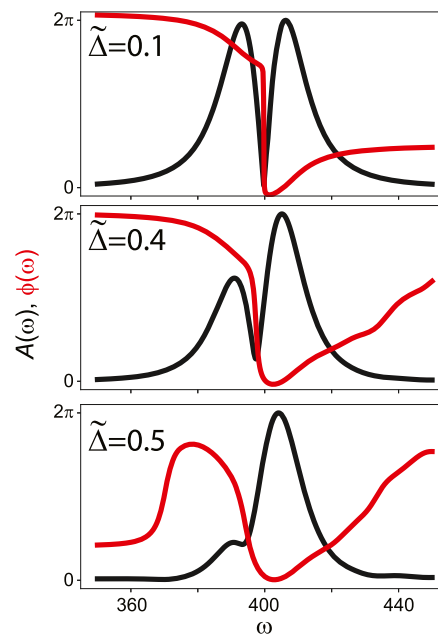

Figure 11. Morse oscillator FCS at $\omega_2 = \omega_{0,1}$ for $\tilde{\Delta} = 0.1$ (top), $\tilde{\Delta} = 0.4$ (middle), and $\tilde{\Delta} = 0.5$ (bottom) for $\lambda = 12$ and $\omega_0^{eff} = 9$ and in which the n and m sums used all 12 bound states.

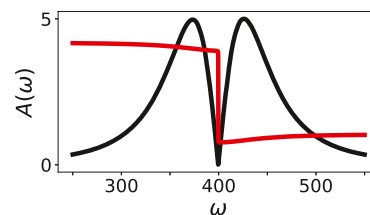**Figure 12.** Morse oscillator FCS at $\omega_2 = \omega_{0,1}$ for $\tilde{\Delta} = 0.1$ for $\lambda = 12$ and $\omega_0^{eff} = 9$ and in which the n and m sums used all 12 bound states. Here, the dephasing was set to $\gamma = 10\omega_0^{eff}$, which recovers the harmonic result for the classical window.

asymmetric peak heights readily arise from anharmonicity of the potentials in contrast to the negligible or minimal asymmetry that arises from harmonic potentials.

Quantum Beats from an Electronic Dimer. One purpose of this work is to develop an understanding of the phase and amplitude profiles in FCS so that researchers can distinguish the underlying physical origin of the measured quantum beats. Therefore, we study a purely electronic dimer. Previous authors have detailed the nonlinear response arising from this system.[5,58,59]

Briefly, the system is composed of two potentially distinct electronic two-level systems, $|a\rangle$ and $|b\rangle$. The system Hamiltonian is given by

$$\hat{H}_s = \hbar\omega_a|e_a\rangle\langle e_a| + \hbar\omega_b|e_b\rangle\langle e_b| + J(\hat{\sigma}_a^+\hat{\sigma}_b^- + \text{H. c. }) \quad (21)$$

where $\hbar\omega_a$ and $\hbar\omega_b$ are the excited-state energies of the two systems, J is the coupling energy, $\hat{\sigma}_i^+ = |e_i\rangle\langle g_i|$ and $\hat{\sigma}_i^- = |g_i\rangle\langle e_i|$, $i = \{a, b\}$, and H.c. stands for Hermitian conjugate. For the important case of a homodimer, one sets $\omega_a = \omega_b$. On this basis, the transition-dipole moment operator is given by

$$\hat{\mu}_i = \mu_i(|e_i\rangle\langle g_i| + \text{H. c. }) \quad (22)$$

The $\{a, b\}$ basis is typically known as the *site basis*, in contrast to the eigenbasis of the Hamiltonian, which is typically known as the *exciton basis*, given here as $\{|\alpha\rangle, |\beta\rangle\}$. The exciton basis is written as

$$\hat{H}_s = \hbar\omega_\alpha|\alpha\rangle\langle\alpha| + \hbar\omega_\beta|\beta\rangle\langle\beta| + \hbar\omega_f|f\rangle\langle f| \quad (23)$$

Here, we have set the composite ground-state energy to zero and the doubly excited state as the sum, $\hbar\omega_f = \omega_a + \omega_b$. The exciton energies are given by

$$\omega_{\alpha/\beta} = \frac{1}{2}[(\omega_a + \omega_b) \pm (\omega_a - \omega_b)$$
$$\sec(\arctan(J/\hbar(\omega_a - \omega_b)/2))] \qquad (24)$$

The third-order response functions[5,59,60] that contain quantum-beat signals are

$$R_i^{(3)}(\tau_1, \tau_2, \tau_3) \propto e^{-i\omega_\beta\tau_1}e^{-i\omega_{\beta,\alpha}\tau_2}e^{-i\omega_\beta\tau_3} \qquad (25a)$$

$$R_{ii}^{(3)}(\tau_1, \tau_2, \tau_3) \propto e^{-i\omega_\alpha\tau_1}e^{-i\omega_{\alpha,\beta}\tau_2}e^{-i\omega_\alpha\tau_3} \qquad (25b)$$

$$R_{iii}^{(3)}(\tau_1, \tau_2, \tau_3) \propto e^{+i\omega_\alpha\tau_1}e^{-i\omega_{\beta,\alpha}\tau_2}e^{-i\omega_\beta\tau_3} \qquad (25c)$$

$$R_{iv}^{(3)}(\tau_1, \tau_2, \tau_3) \propto e^{+i\omega_\beta\tau_1}e^{-i\omega_{\alpha,\beta}\tau_2}e^{-i\omega_\alpha\tau_3} \qquad (25d)$$

The total transient-absorption signal under spectrally resolved detection is the sum of these terms for $\tau_1 = 0$ followed by Fourier transformation over τ_3 to yield the detection frequency variable ω

$$M(\omega, \tau_2) = \mathscr{F}_{\tau_3}\left[\sum_{k=i}^{iv} R_k^{(3)}(\tau_1 = 0, \tau_2, \tau_3)\right]_\omega$$
$$\propto \frac{e^{-i\omega_{\beta,\alpha}\tau_2}}{(\omega_2 - \omega_\beta)^2 - \gamma} + \frac{e^{-i\omega_{\alpha,\beta}\tau_2}}{(\omega_2 - \omega_\alpha)^2 - \gamma}. \qquad (26)$$

Therefore, the coherence spectrum at frequency $\omega_{\beta,\alpha}$ resulting from Fourier transformation over time interval τ_2 and taking the real part of the complex-valued function is given by

$$M(\omega; \omega_{\beta,\alpha}) = \mathrm{Re}\left[\mathscr{F}_{\tau_2}[M(\omega; \tau_2)]\big|_{\omega_{\beta,\alpha}}\right]$$
$$\propto \frac{1}{(\omega_2 - \omega_\beta)^2 - \gamma} + \frac{1}{(\omega_2 - \omega_\alpha)^2 - \gamma}, \qquad (27)$$

where $\omega_{\beta,\alpha} = (E_\beta - E_\alpha)/\hbar$, the electronic coherence frequency.

The key distinction between this expression and those of the vibrational models is that here the two Lorentzian terms are summed rather than subtracted. This leads to constructive interference of the peaks, and therefore there is no relative phase shift. In Figure 13, we present FCS for an electronic homodimer under three distinct levels of coupling, J, and constant dephasing, γ. The absence of an amplitude node when $J < \gamma$ indicates the constructive interference. When $J > \gamma$, there are two distinct peaks having no relative phase shift. In sum, the absence of the amplitude node and phase shift appears to be a diagnostic for electronic coherence in excitonic systems.

CONCLUSIONS

We have derived and presented the analytic expression for the FCS arising from models including harmonic and anharmonic oscillators as well as an electronic dimer. These models will be useful for assigning the microscopic origins of quantum-beat signals in transient-absorption spectroscopy measurements conducted with femtosecond laser pulses. We envision that, after performing measurements and accounting for pulse chirp, researchers will be able to fit the measured FCS to the expressions and extract values for the microscopic parameters of the molecular potential-energy surfaces. Future theoretical work could evaluate niche cases that we have neglected. One key example is a vibrational dimer having electronic coupling; such
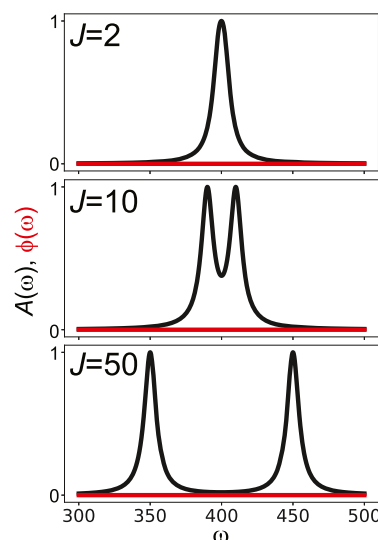

Figure 13. Femtosecond coherence spectrum for an electronic homodimer under three indicated levels of electronic coupling, J, for $\omega_a = \omega_b = 400$ and $\gamma = 5$. There is no amplitude node or phase shift between the two peaks.

systems indeed are of prime importance for molecular excitonic applications.

AUTHOR INFORMATION

Corresponding Author

Daniel B. Turner − *Micron School for Materials Science and Engineering, Boise State University, Boise, Idaho 83725, United States;* ● orcid.org/0000-0002-3148-5317; Email: danielturner926@boisestate.edu

Author

Paul C. Arpin − *Department of Physics, California State University, Chico, Chico, California 95929, United States*

Complete contact information is available at:
https://pubs.acs.org/10.1021/acs.jpca.0c10807

Notes

The authors declare no competing financial interest.

REFERENCES

(1) Fragnito, H. L.; Bigot, J.-Y.; Becker, P. C.; Shank, C. V. Evolution of the Vibronic Absorption Spectrum in a Molecule Following Impulsive Excitation with a 6 fs Optical Pulse. *Chem. Phys. Lett.* **1989**, *160*, 101−104.

(2) Pollard, W. T.; Lee, S. Y.; Mathies, R. A. Wave Packet Theory of Dynamic Absorption Spectra in Femtosecond Pump-Probe Experiments. *J. Chem. Phys.* **1990**, *92*, 4012−4029.

(3) Pollard, W. T.; Dexheimer, S. L.; Wang, Q.; Peteanu, L. A.; Shank, C. V.; Mathies, R. A. Theory of Dynamic Absorption Spectroscopy of Nonstationary States. 4. Application to 12-fs Resonant Impulsive Raman Spectroscopy of Bacteriorhodopsin. *J. Phys. Chem.* **1992**, *96*, 6147−6158.

(4) Bardeen, C. J.; Wang, Q.; Shank, C. V. Selective Excitation of Vibrational Wave Packet Motion Using Chirped Pulses. *Phys. Rev. Lett.* **1995**, *75*, 3410−3413.

(5) Mukamel, S. *Principles of Nonlinear Optical Spectroscopy*; Oxford University Press: New York, 1995.

(6) Shah, J. *Ultrafast Spectroscopy of Semiconductors and Semiconductor Nanostructures*; Springer-Verlag, 1999.

(7) Vos, M. H.; Rappaport, F.; Lambry, J.-C.; Breton, J.; Martin, J.-L. Visualization of Coherent Nuclear Motion in a Membrane Protein by Femtosecond Spectroscopy. *Nature* **1993**, *363*, 320−325.

(8) Chachisvilis, M.; Fidder, H.; Sundström, V. Electronic Coherence in Pseudo Two-Colour Pump−Probe Spectroscopy. *Chem. Phys. Lett.* **1995**, *234*, 141−150.

(9) McClure, S. D.; Turner, D. B.; Arpin, P. C.; Mirkovic, T.; Scholes, G. D. Coherent Oscillations in the PC577 Cryptophyte Antenna Occur in the Excited Electronic State. *J. Phys. Chem. B* **2014**, *118*, 1296−1308.

(10) Arpin, P. C.; Turner, D. B.; McClure, S. D.; Jumper, C. C.; Mirkovic, T.; Challa, J. R.; Lee, J.; Teng, C. Y.; Green, B. R.; Wilk, K. E.; et al. Spectroscopic Studies of Cryptophyte Light Harvesting Proteins: Vibrations and Coherent Oscillations. *J. Phys. Chem. B* **2015**, *119*, 10025−10034.

(11) Rosca, F.; Kumar, A. T. N.; Ionascu, D.; Sjodin, T.; Demidov, A. A.; Champion, P. M. Wavelength Selective Modulation in Femtosecond Pump−Probe Spectroscopy and Its Application to Heme Proteins. *J. Chem. Phys.* **2001**, *114*, 10884.

(12) Mathies, R.; Brito Cruz, C.; Pollard, W.; Shank, C. Direct Observation of the Femtosecond Excited-State cis-trans Isomerization in Bacteriorhodopsin. *Science* **1988**, *240*, 777−779.

(13) Wang, Q.; Schoenlein, R.; Peteanu, L.; Mathies, R.; Shank, C. Vibrationally Coherent Photochemistry in the Femtosecond Primary Event of Vision. *Science* **1994**, *266*, 422−424.

(14) Bardeen, C. J.; Wang, Q.; Shank, C. V. Femtosecond Chirped Pulse Excitation of Vibrational Wave Packets in LD690 and Bacteriorhodopsin. *J. Phys. Chem. A* **1998**, *102*, 2759−2766.

(15) Kobayashi, T.; Saito, T.; Ohtani, H. Real-Time Spectroscopy of Transition States in Bacteriorhodopsin During Retinal Isomerization. *Nature* **2001**, *414*, 531−534.

(16) Kahan, A.; Nahmias, O.; Friedman, N.; Sheves, M.; Ruhman, S. Following Photoinduced Dynamics in Bacteriorhodopsin with 7-fs Impulsive Vibrational Spectroscopy. *J. Am. Chem. Soc.* **2007**, *129*, 537−546.

(17) Johnson, P. J. M.; Halpin, A.; Morizumi, T.; Brown, L. S.; Prokhorenko, V. I.; Ernst, O. P.; Dwayne Miller, R. J. The Photocycle and Ultrafast Vibrational Dynamics of Bacteriorhodopsin in Lipid Nanodiscs. *Phys. Chem. Chem. Phys.* **2014**, *16*, 21310−21320.

(18) Liebel, M.; Schnedermann, C.; Bassolino, G.; Taylor, G.; Watts, A.; Kukura, P. Direct Observation of the Coherent Nuclear Response after the Absorption of a Photon. *Phys. Rev. Lett.* **2014**, *112*, 238301.

(19) Liebel, M.; Schnedermann, C.; Wende, T.; Kukura, P. Principles and Applications of Broadband Impulsive Vibrational Spectroscopy. *J. Phys. Chem. A* **2015**, *119*, 9506−9517.

(20) Müller, M. G.; Lindner, I.; Martin, I.; Gärtner, W.; Holzwarth, A. R. Femtosecond Kinetics of Photoconversion of the Higher Plant Photoreceptor Phytochrome Carrying Native and Modified Chromophores. *Biophys. J.* **2008**, *94*, 4370−4382.

(21) Bizimana, L. A.; Carbery, W. P.; Gellen, T. A.; Turner, D. B. Signatures of Herzberg−Teller Coupling in Three-Dimensional Electronic Spectroscopy. *J. Chem. Phys.* **2017**, *146*, 084311.

(22) Bizimana, L. A.; Epstein, J.; Brazard, J.; Turner, D. B. Conformational Homogeneity in the P_r Isomer of Phytochrome Cph1. *J. Phys. Chem. B* **2017**, *121*, 2622−2630.

(23) Bizimana, L. A.; Epstein, J.; Turner, D. B. Inertial Water Response Dominates Protein Solvation Dynamics. *Chem. Phys. Lett.* **2019**, *728*, 1−5.

(24) Kobayashi, T.; Wang, Z.; Otsubo, T. Classification of Dynamic Vibronic Couplings in Vibrational Real-Time Spectra of a Thiophene Derivative by Few-Cycle Pulses. *J. Phys. Chem. A* **2007**, *111*, 12985−12994.

(25) Du, J.; Wang, Z.; Feng, W.; Yoshino, K.; Kobayashi, T. Simultaneous Measurement of Electronic and Vibrational Dynamics to Clarify a Geometrical Relaxation Process in a Conjugated Polymer. *Phys. Rev. B: Condens. Matter Mater. Phys.* **2008**, *77*, 195205.

(26) Kano, H.; Saito, T.; Kobayashi, T. Observation of Herzberg-Teller-Type Wave Packet Motion in Porphyrin J-Aggregates Studied by sub-5-fs Spectroscopy. *J. Phys. Chem. A* **2002**, *106*, 3445−3453.

(27) Jonas, D. M.; Fleming, G. R. *Ultrafast Processes in Ultrafast Processes in Chemistry and Photobiology*; El-Sayed, M. A., Tanaka, I., Molin, Y., Eds.; Chemistry for the 21st Century; Blackwell Scientific Publications: Oxford, 1995; p 225.

(28) Rafiq, S.; Dean, J. C.; Scholes, G. D. Observing Vibrational Wavepackets During an Ultrafast Electron Transfer Reaction. *J. Phys. Chem. A* **2015**, *119*, 11837−11846.

(29) Brazard, J.; Bizimana, L. A.; Gellen, T.; Carbery, W. P.; Turner, D. B. Experimental Detection of Branching at a Conical Intersection in a Highly Fluorescent Molecule. *J. Phys. Chem. Lett.* **2016**, *7*, 14−19.

(30) Wand, A.; Kallush, S.; Shoshanim, O.; Bismuth, O.; Kosloff, R.; Ruhman, S. Chirp Effects on Impulsive Vibrational Spectroscopy: A Multimode Perspective. *Phys. Chem. Chem. Phys.* **2010**, *12*, 2149−2163.

(31) Jonas, D. M.; Bradforth, S. E.; Passino, S. A.; Fleming, G. R. Femtosecond Wavepacket Spectroscopy: Influence of Temperature, Wavelength, and Pulse Duration. *J. Phys. Chem.* **1995**, *99*, 2594−2608.

(32) Yang, T.-S.; Chang, M.-S.; Chang, R.; Hayashi, M.; Lin, S. H.; Vöhringer, P.; Dietz, W.; Scherer, N. F. Femtosecond Pump-Probe Study of Molecular Vibronic Structures and Dynamics of a Cyanine Dye in Solution. *J. Chem. Phys.* **1999**, *110*, 12070−12081.

(33) Scherer, N. F.; Jonas, D. M.; Fleming, G. R. Femtosecond Wave Packet and Chemical Reaction Dynamics of Iodine in Solution: Tunable Probe Study of Motion Along the Reaction Coordinate. *J. Chem. Phys.* **1993**, *99*, 153−168.

(34) Bishop, M. M.; Roscioli, J. D.; Ghosh, S.; Mueller, J. J.; Shepherd, N. C.; Beck, W. F. Vibrationally Coherent Preparation of the Transition State for Photoisomerization of the Cyanine Dye Cy5 in Water. *J. Phys. Chem. B* **2015**, *119*, 6905−6915.

(35) Dean, J. C.; Rafiq, S.; Oblinsky, D. G.; Cassette, E.; Jumper, C. C.; Scholes, G. D. Broadband Transient Absorption and Two-Dimensional Electronic Spectroscopy of Methylene Blue. *J. Phys. Chem. A* **2015**, *119*, 9098−9108.

(36) Liebel, M.; Kukura, P. Broad-Band Impulsive Vibrational Spectroscopy of Excited Electronic States in the Time Domain. *J. Phys. Chem. Lett.* **2013**, *4*, 1358−1364.

(37) Lüer, L.; Gadermaier, C.; Crochet, J.; Hertel, T.; Brida, D.; Lanzani, G. Coherent Phonon Dynamics in Semiconducting Carbon Nanotubes: A Quantitative Study of Electron-Phonon Coupling. *Phys. Rev. Lett.* **2009**, *102*, 127401.

(38) Rury, A. S.; Sorenson, S. A.; Dawlaty, J. M. Coherent Vibrational Probes of Hydrogen Bond Structure Following Ultrafast Electron Transfer. *J. Phys. Chem. C* **2016**, *120*, 21740−21750.

(39) Rury, A. S.; Sorenson, S. A.; Dawlaty, J. M. Evidence of Ultrafast Charge Transfer Driven by Coherent Lattice Vibrations. *J. Phys. Chem. Lett.* **2017**, *8*, 181−187.

(40) Thouin, F.; Valverde-Chávez, D. A.; Quarti, C.; Cortecchia, D.; Bargigia, I.; Beljonne, D.; Petrozza, A.; Silva, C.; Srimath Kandada, A. R. Phonon Coherences Reveal the Polaronic Character of Excitons in Two-Dimensional Lead Halide Perovskites. *Nat. Mater.* **2019**, *18*, 349−356.

(41) Pollard, W. T.; Fragnito, H. L.; Bigot, J.-Y.; Shank, C.-V.; Mathies, R. A. Quantum-Mechanical Theory for 6 fs Dynamic Absorption Spectroscopy and Its Application to Nile Blue. *Chem. Phys. Lett.* **1990**, *168*, 239−245.

(42) Pollard, W. T.; Mathies, R. A. Analysis of Femtosecond Dynamic Absorption Spectra of Nonstationary States. *Annu. Rev. Phys. Chem.* **1992**, *43*, 497−523.

(43) Kumar, A. T. N.; Rosca, F.; Widom, A.; Champion, P. M. Investigations of Amplitude and Phase Excitation Profiles in Femtosecond Coherence Spectroscopy. *J. Chem. Phys.* **2001**, *114*, 701−724.

(44) Cina, J. A.; Kovac, P. A.; Jumper, C. C.; Dean, J. C.; Scholes, G. D. Ultrafast Transient Absorption Revisited: Phase-Flips, Spectral Fingers, and Other Dynamical Features. *J. Chem. Phys.* **2016**, *144*, 175102.

(45) Turner, D. B.; Arpin, P. C. Basis Set Truncation Further Clarifies Vibrational Coherence Spectra. *Chem. Phys.* **2020**, *539*, 110948.

(46) Musser, A. J.; Liebel, M.; Schnedermann, C.; Wende, T.; Kehoe, T. B.; Rao, A.; Kukura, P. Evidence for Conical Intersection Dynamics Mediating Ultrafast Singlet Exciton Fission. *Nat. Phys.* **2015**, *11*, 352−357.

(47) Breen, I.; Tempelaar, R.; Bizimana, L. A.; Kloss, B.; Reichman, D. R.; Turner, D. B. Triplet Separation Drives Singlet Fission After Femtosecond Correlated Triplet Pair Production in Rubrene. *J. Am. Chem. Soc.* **2017**, *139*, 11745−11751.

(48) Cao, J.; Cogdell, R. J.; Coker, D. F.; Duan, H.-G.; Hauer, J.; Kleinekathöfer, U.; Jansen, T. L. C.; Mančal, T.; Miller, R. J. D.; Ogilvie, J. P.; et al. Quantum Biology Revisited. *Sci. Adv.* **2020**, *6*, No. eaaz4888.

(49) Fitzpatrick, C.; Odhner, J. H.; Levis, R. J. Spectral Signatures of Ground- and Excited-State Wavepacket Interference after Impulsive Excitation. *J. Phys. Chem. A* **2020**, *124*, 6856−6866.

(50) Turner, D. B.; Wilk, K. E.; Curmi, P. M. G.; Scholes, G. D. Comparison of Electronic and Vibrational Coherence Measured by Two-Dimensional Electronic Spectroscopy. *J. Phys. Chem. Lett.* **2011**, *2*, 1904−1911.

(51) Bizimana, L. A.; Brazard, J.; Carbery, W. P.; Gellen, T.; Turner, D. B. Resolving Molecular Vibronic Structure using High-Sensitivity Two-Dimensional Electronic Spectroscopy. *J. Chem. Phys.* **2015**, *143*, 164203.

(52) Hybl, J. D.; Albrecht Ferro, A.; Jonas, D. M. Two-Dimensional Fourier Transform Electronic Spectroscopy. *J. Chem. Phys.* **2001**, *115*, 6606−6622.

(53) Yan, Y. J.; Mukamel, S. Femtosecond Pump-Probe Spectroscopy of Polyatomic Molecules in Condensed Phases. *Phys. Rev. A* **1990**, *41*, 6485−6504.

(54) Yan, Y. J.; Fried, L. E.; Mukamel, S. Ultrafast pump-probe spectroscopy: femtosecond dynamics in Liouville space. *J. Phys. Chem.* **1989**, *93*, 8149−8162.

(55) Dahl, J. P.; Springborg, M. The Morse Oscillator in Position Space, Momentum Space, and Phase Space. *J. Chem. Phys.* **1988**, *88*, 4535−4547.

(56) Iachello, F.; Ibrahim, M. Analytic and Algebraic Evaluation of Franck−Condon Overlap Integrals. *J. Phys. Chem. A* **1998**, *102*, 9427−9432.

(57) Farfan, C. A.; Turner, D. B. Interference Among Multiple Vibronic Modes in Two-Dimensional Electronic Spectroscopy. *Mathematics* **2020**, *8*, 157.

(58) Hamm, P.; Zanni, M. T. *Concepts and Methods of 2D Infrared Spectroscopy*; Cambridge University Press, 2011.

(59) Brańczyk, A. M.; Turner, D. B.; Scholes, G. D. Crossing Disciplines - A View on Two-Dimensional Optical Spectroscopy. *Ann. Phys.* **2014**, *526*, 31−49.

(60) Turner, D. B.; Howey, D. J.; Sutor, E. J.; Hendrickson, R. A.; Gealy, M. W.; Ulness, D. J. Two-Dimensional Electronic Spectroscopy Using Incoherent Light: Theoretical Analysis. *J. Phys. Chem. A* **2013**, *117*, 5926−5954.